Geomorphology 435 (2023) 108766

Contents lists available at ScienceDirect

Geomorphology

journal homepage: www.journals.elsevier.com/geomorphology

Quantifying geomorphic change in Andean river valleys using UAV-PPK-SfM techniques: An example from the western Peruvian Andes

Miluska A. Rosas [a,b,c,*], François Clapuyt [a,d], Willem Viveen [c], Veerle Vanacker [a]

[a] Earth and Life Institute, Centre for Earth and Climate Research, Université catholique de Louvain, Place Louis Pasteur 3, L4.03.08, 1348 Louvain la Neuve, Belgium
[b] GERDIS, GEOSED, Departamento de Ingeniería, Pontificia Universidad Católica del Perú, Lima, Perú
[c] Grupo de Investigación en Geología Sedimentaria, Especialidad de Ingeniería Geológica, Departamento de Ingeniería, Pontificia Universidad Católica del Perú, Lima, Peru
[d] Fonds de la Recherche Scientifique FRS-FNRS, Brussels, Belgium

A R T I C L E I N F O

Keywords:
Erosion
Andes
Peru
Topographic change
4D monitoring

A B S T R A C T

The western Peruvian region is prone to erosion and geomorphic change. Extreme precipitation events lead to rapid change in river channel and floodplain morphology due to bank erosion and debris flows delivering detrital material to the fluvial system. Monitoring geomorphic events and their associated topographic changes at high spatial and temporal resolutions remains a challenge. Here, we used an Uncrewed Aerial Vehicle - Post-Processing Kinematic - Structure from Motion (UAV-PPK-SfM) approach that includes co-registration of point clouds by using relative Ground Control Points (GCPs). This workflow adjusts each elevation model to a reference model using invariant features that did not change their position or form over time. We applied this technique to monitor landscape change (2019–2021) in an area of 0.3 km^2 located in the Cañete River basin. Our results showed that a minimum observable elevation change of 0.56 m (95 % confidence interval) can be achieved using this workflow, beyond which an actual elevation change can be separated from systematic error. Using object-based classification techniques on the aerial images, we separated geomorphic dynamics from land cover changes. This allowed us to isolate the effect of geomorphic processes, and quantify rates related to gully erosion, river scouring, bank erosion, and sediment deposition. Within the study area, a hotspot of geomorphic change corresponded to an ephemeral tributary channel. The gully channel incising an alluvial fan is highly dynamic, showing bank erosion of 0.75 to 3.2 m and net export of 37 m^3 of sediment in the 25-month study period. Given that the monitoring period did not include high intensity rainfall events, the study illustrates how geomorphic activity in ungauged Andean river basins, such as the Cañete valley, may be considerably underestimated in literature.

1. Introduction

Mountainous environments in the dry Andean region are intrinsically prone to erosion processes, i.e. gullies or landslides, due to their accentuated topography and infrequent, but large, rainfall events (Molina et al., 2008; Clark et al., 2016; Morera et al., 2017). The rugged western Peruvian Andes (4°S–18°S) is located between the Pacific coastal plain and the central Andes and is characterised by elevations of up to 5000 m and up-to 3000 m deep, and incised, braided, river valleys (Schildgen et al., 2007). The alluvial plains are formed by the accumulation of sediments sourced from the Andean region and delivered to the stream network by ephemeral channels and gullies that are activated during seasonal extreme rainfall events (Morera et al., 2017). For the Tropical Andes, previous studies reported specific sediment yield between 5 and 2300 t km^{-2} yr^{-1} (Restrepo et al., 2009; Latrubesse and Restrepo, 2014; Vanacker et al., 2022; Rosas et al., 2023).

The dry Andes is characterised by a high variability in precipitation rates associated with the El Niño Southern Oscillation (ENSO) (Mettier et al., 2009; Tote et al., 2011). The mean annual precipitation ranges between 16 and 90 mm yr^{-1} (Rau et al., 2017), but can increase by 4 to 60 times during ENSO events (Morera et al., 2017). Extreme precipitation events trigger rapid soil erosion, mass movement and bank erosion (Molina et al., 2008; Tote et al., 2011; Clark et al., 2016), that deliver material to the river system and lead to rare, but catastrophic, flooding and rapid changes in river channel and floodplain morphology (INGEMMET, 2013; Restrepo et al., 2020). Sediment yields during

* Corresponding author at: Earth and Life Institute, Centre for Earth and Climate Research, Université catholique de Louvain, Belgium.
E-mail address: miluska.rosas@pucp.pe (M.A. Rosas).

https://doi.org/10.1016/j.geomorph.2023.108766
Received 7 December 2021; Received in revised form 19 May 2023; Accepted 28 May 2023
Available online 30 May 2023
0169-555X/

moderate ENSO events are estimated to be 5 to 11 times the rates during normal rainy seasons (Tote et al., 2011), and increases up-to 60-times are reported during extreme events resulting in sediment fluxes up to 1000 and 3000 t km^{-2} yr^{-1} (Morera et al., 2017).

Global change and anthropogenic disturbances further increase the pressure on this fragile environment (Rau et al., 2018; Vanacker et al., 2022). In Peru, around 16,400 km^2 of land was converted for agricultural use during the 1994–2012 period (Morris, 2017). Land use changes including the development of irrigation systems and expansion of cropland are potentially linked to geomorphic and landscape changes (Vanacker et al., 2003, 2005; Lacroix et al., 2020) and can further intensify land degradation when the agricultural practices are not sustainable (Barrowclough et al., 2016; FAO and CAF, 2016).

Given the dynamic geomorphology of the western Peruvian river valleys and their exposure to accelerated environmental change, there is an urgent need to (i) identify hotspots of geomorphic change and (ii) quantify erosion, sediment production and delivery to the channel network (Aber et al., 2019). In the last decade, geomorphic studies in this region mostly focused on large-scale erosion patterns as result of water erosion processes or mass movements (Mettier et al., 2009; Höfle et al., 2013; Zerathe et al., 2016; Luque et al., 2020; Rosas et al., 2023). The study of specific erosion processes or geomorphic events (e.g., flash floods or debris flows) that require observational data at high spatio-temporal resolution (i.e., decimetric to centimetric resolution) remains a challenge due to limited accessibility. Because of a scarcity of data on individual geomorphic events, it is not yet possible to answer how fast, when, and how sediment is produced and delivered to the channel network.

The availability of high resolution satellite and aerial data-sources, and technological advances in image processing have facilitated landscape monitoring over the last 20 years (Tarolli, 2014; Passalacqua et al., 2015). The use of photogrammetric Structure from Motion (SfM) and multi-view stereo (MVS) algorithms, based on images acquired from an Uncrewed Aerial Vehicle (UAV), is now considered an established method for repeated, high-resolution topographic surveys in remote and rugged terrain (Eltner et al., 2016; James et al., 2019). Using a UAV-SfM framework, time series of high-resolution digital surface models (DSM) can be produced for four dimensional (4D) analysis of geomorphic processes (Clapuyt et al., 2017; Huang et al., 2017; Eker et al., 2018; Hendrickx et al., 2020; Cândido et al., 2020).

Recent advances include direct georeferencing of UAV images with coordinates measured by differential Global Navigation Satellite System (GNSS) measurements in real-time kinematic (RTK) or post-processing kinematic (PPK) mode. The workflow with a combined use of UAV, PPK-GNSS, and SfM-MVS photogrammetry, hereafter referred to as UAV-PPK-SfM, can provide consistent and repeatable data with a centimetre level uncertainty, using a single or few Ground Control Points (GCPs; Forlani et al., 2018; Zhang et al., 2019; Kalacska et al., 2020). This technique provides robust solutions when low uncertainty and high temporal resolution are required, also in areas where a regular spacing and distribution of GCPs is precluded due to the limited accessibility. However, published uncertainty assessments of the UAV-PPK-SfM workflow are restricted to hectometre-sized areas characterised by low topographic relief (e.g., Zhang et al., 2019; Cucchiaro et al., 2020; Pingel et al., 2021). Only recently, efforts have been made to test the methodology in more complex topography (Notti et al., 2021; Žabota and Kobal, 2021).

This study attempts to provide quantitative data on geomorphic process rates for western Peruvian river valleys and goes beyond the current state of the art by evaluating the UAV-PPK-SfM workflow for rugged and complex topography. A dynamic landscape was selected for this study and was monitored for 4D changes over the period 2019 to 2021. This period was characterised by normal precipitation rates and absence of El Niño events. Therefore, the potential of UAV-PPK-SfM techniques for monitoring average geomorphic activity in this and, potentially, other similar (semi-)arid mountainous areas was fully explored.

2. Study area

The study area (0.3 km^2) is located in the Cañete River catchment of the western Peruvian Andes, 180 km south of Lima city (Fig. 1), and just 1 km east of the small town of Zuñiga. The braided Cañete River crosses the area in a northeast-southwest direction and creates a floodplain of ~28 m wide. The riverbed material is heterogeneous and contains sand and gravels ranging in size from 0.01 to ~2.5 m of diameter. One fluvial terrace with an elevation of ~5 m above the floodplain is present at the south of the valley (Viveen et al., 2022). The valley rims are situated at ~950 m above sea level (a.s.l.), and the floodplain at ~825 m a.s.l., with a maximum elevation difference of ~125 m. The slope gradient of the valley floor ranges from 0° to 5.5°. The study area is centered on the confluence of an ephemeral stream with the Cañete River. At this confluence, situated in the south part of the study area, a large, coarse-grained alluvial fan is present with an area of 0.02 km^2 and slope gradient increasing from 5.5° at the confluence to over 30° in the upper part of the fan. The regional lithology corresponds to acid plutonic rocks, mainly granodiorites from the Cretaceous, and gravel-grade, unconsolidated, late Quaternary alluvial deposits (Luque et al., 2020). The study area exhibits rapid erosion rates, with specific sediment yields of 318 t km^{-2} yr^{-1} for the Cañete River (Rosas et al., 2020). The region is prone to mass movements including landslides, rock falls and debris flows. Two important events took place in the years 1996 and 2012 and severely affected local infrastructure. Likewise, riverbank erosion and debris flows are frequently reported in local newspapers and grey literature (INGEMMET, 2013; INGEMMET, 2022).

The flat areas corresponding to the inactive floodplain, fluvial terrace and top of the most distal parts of the alluvial fan are used for agriculture. Vineyards are present, as well as a variety of fruit trees such as mangos, citrus trees and avocados. In the region, there is a strong increase in informal settlements, as well as road infrastructure over the last 6 yr. The active floodplain is covered by grasses and shrubs. The medial and proximal part of the alluvial fan are bare, as well as the steep valley sides. The study area experiences arid weather conditions with a mean annual precipitation of 16 mm yr^{-1} (average over period 1965–2017), increasing up to 95 mm yr^{-1} or more during El Niño events. Year-round temperature oscillates between 15 °C and 25 °C (Aybar et al., 2020).

3. Materials and methods

3.1. Data acquisition

3.1.1. Uncrewed Aerial Vehicle survey

The study area was surveyed during three field campaigns: (1) in February 2019 at the end of the rainy season, (2) in July 2019 during the dry season, and (3) in March 2021 after the rainy season. The UAV used was a DJI Phantom 3 Professional equipped with a GoPro Hero 3 camera (12 megapixels, 4000 × 3000 pixels) having a focal length of 2.92 mm (f/2.8 aperture). We used the highest camera resolution (12 megapixels) in order to minimize distortions caused by the fish-eye lens. The approximate sensor size was 5.8 mm × 4.3 mm. We planned 12 flights that overlapped each other in order to cover the entire study area. The flight plan followed a fishnet pattern with two different camera orientations: nadir- and oblique-oriented (~30° relative to nadir), resulting in several flights for the same area to reduce systematic errors (e. g. dome effect) in the derived 3D point clouds (James and Robson, 2014; Nesbit and Hugenholtz, 2019). We set the average flight speed at 4 m s^{-1} and a constant flight height of 40 m above ground. The typical flight duration was 15 min and covered a flight distance of 1.3 km on average. The camera trigger interval was set at 4 s, in order to obtain an overlap of 80 % between consecutive images, and a centimetre-level ground sampling distance. The flights were designed to detect hotspots of geomorphic

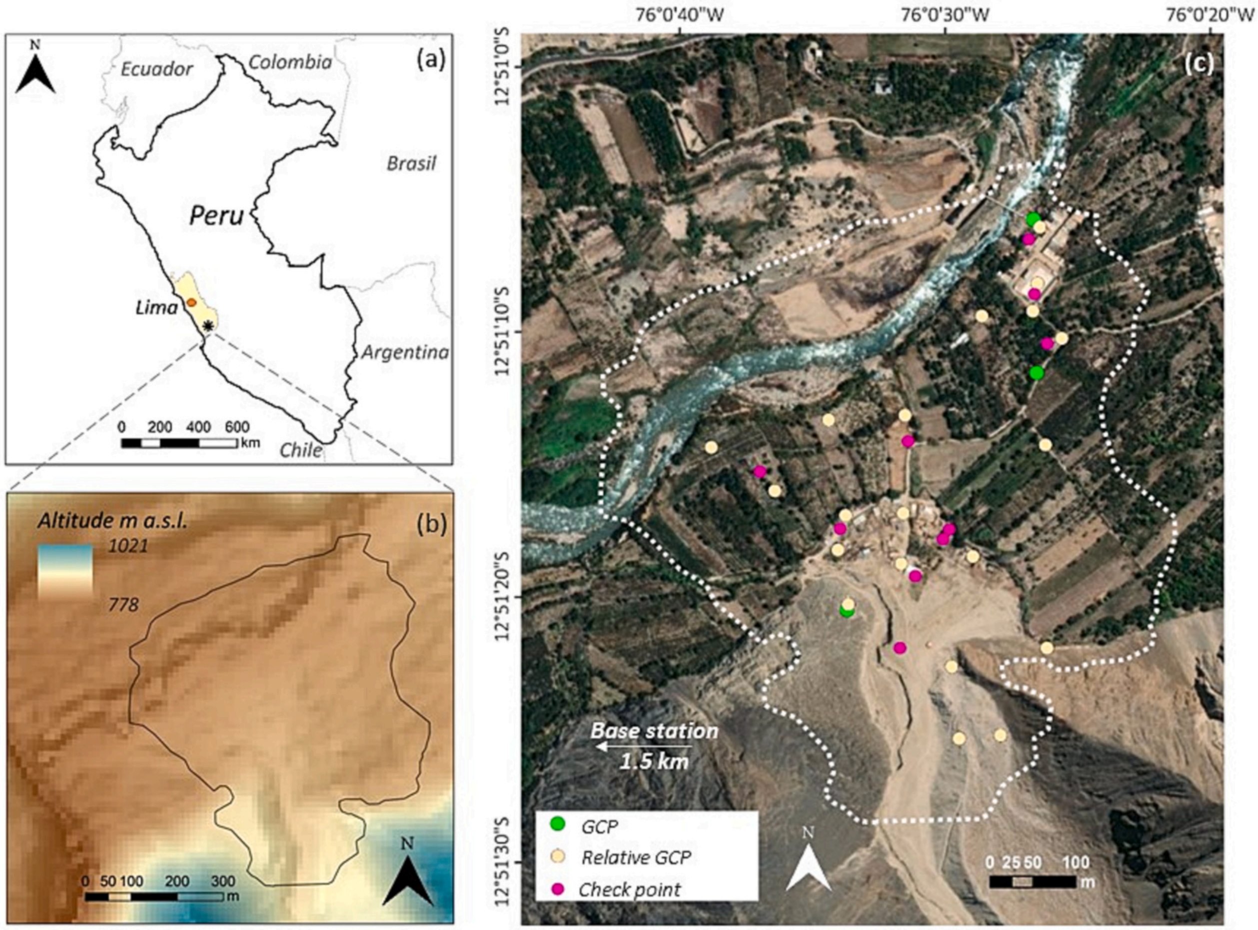

Fig. 1. Location of the study area (a) in the Peruvian western Andes. (b) Digital elevation model (WorldDEM™ model by Airbus Defence and Space) and (c) orthomosaic of the study area, with indication of location of Ground Control Points (GCPs), relative GCPs and checkpoints. The white, dashed line delimits the surveyed area.

change and to quantify topographic changes as a result of various geomorphic processes including concentrated flow, mass movements and bank erosion, that are expected to be observable at centimetric-level scale. The flight missions were planned with the Autopilot application, for iOS. Respectively 2169, 2236 and 2303 images were taken for the first, second and third surveys.

3.1.2. Geotagging of images

The UAV platform was equipped with a Reach RTK, which is a single-band GNSS RTK receiver, also used by Zhang et al. (2019) with both RTK and PPK capabilities. The receiver antenna was placed right above the camera lens centre to avoid the horizontal offsets, and the vertical offset was 22.5 cm which corresponded to the camera-antenna height. The offset was corrected during the post-processing procedure (Zhang et al., 2019). We used a portable base station, i.e. the RTK GNSS receiver Emlid Reach RS+. This single-band receiver possesses 72 channels and tracks GPS/QZSS, GLONASS, BeiDou, Galileo and SBAS signals. The achievable horizontal and vertical error of the receiver is 7 mm and 14 mm respectively in PPK mode. The base station was set up on a tripod at a fixed reference point with geographic position (Longitude: −76.0219, Latitude: −12.8609, Altitude: 841.408 m). This reference point has been established by Gonzáles-Moradas and Viveen (2020).

The distance between the base station and the UAV flights was ~1.5 km. The camera positions were estimated using the PPK mode during post-processing. The open-source RTKLib software (Takasu and Yasuda, 2009) was used to compute the horizontal coordinates and altitude of each receiver antenna position. High-precision GNSS positioning, and navigation requires proper handling of the carrier phase ambiguity resolution. This is a measure of the geometric range between the satellite and receiver. We verified the consistency of the estimated receiver antenna positions by evaluating different satellite elevation masks (15° and 20°) and two integer ambiguity resolution methods (continuous and fix-and-hold) to avoid false solutions that could otherwise remain undetected. The continuous method estimates the carrier phase biases continuously over the different epochs, while the fix-and-hold method feeds information from one epoch towards the subsequent epoch. No lever arm corrections were included in the camera position adjustment, and only a constant vertical offset (22.5 cm) was considered. As Zhang et al. (2019) discussed, the propagated errors from the small antenna offset of [0, 0, 22.5] cm to the camera position are insignificant, i.e. ~1 cm.

3.1.3. Measurement of absolute and relative ground control points and checkpoints

Three static features were used for the ground control points (GCPs), and they correspond to large boulders or elements of large, hydraulic infrastructure. The geographic coordinates of these 'absolute' GCPs were measured using a Trimble 5800 GPS receiver, and the base station already established by Gonzáles-Moradas and Viveen (2020). The recording time of each GCP was ~30 min. The correction files were provided by the Peruvian Geographic Institute (antenna: LI04 Pucusana; international code: 42245M001) and correction was done during post-processing. The coordinate system used was the projected Universal Transverse Mercator (UTM) zone 18S based on the datum World

Geodetic System 1984 (WGS84). We obtained millimetric errors for the GCPs, with horizontal and vertical errors smaller than 1 mm (see S1 for more details).

The second survey (July 2019) was selected as the reference model for the other two surface reconstructions (February 2019 and March 2021). On the reference model, we identified invariant local features such as large boulders or elements of solid hydraulic or civil infrastructure that were visible on the two other models. These invariant local features were then used as 'relative' GCPs. We extracted the geographic coordinates and altitude of the relative GCPs from the automatic matching points generated by Pix4D in the first step of the SfM workflow (see Section 3.2.1). Subsequently, the relative GCPs were included in the SfM processing to co-register the other two models (Fig. 1). Similar to the relative GCPs, checkpoints were identified in the reference DSM model as invariant local features, i.e., big rocks or human infrastructure. Checkpoints were used to estimate the individual DSM model error (SDE), and subsequently, the propagated error and the probability of the DSM of difference (DoD) (Sections 3.2.2 and 3.3.1).

3.2. Data processing: photogrammetric workflow

3.2.1. Structure from motion processing

The SfM workflow was carried out in the Pix4Dmapper software (Pix4Dmapper, 2021) in order to reconstruct the preliminary DSMs of the study area for the three flight campaigns. We processed all the images from all flights of each survey to obtain three raw data outputs: the 3D dense point cloud, the orthomosaic and the digital surface model of the surveyed area based on the geotagged images. The first step of the SfM workflow was image alignment by detecting matching points on overlapping images. We set the camera calibration parameters with linear rolling shutter and fish-eye lens to minimize the 'dome effect', which is a systematic surface error based on the lens distortion parameters and the inaccuracy in their calculation (Wackrow and Chandler, 2008; James and Robson, 2014). After the addition of GCPs (absolute and relative), we re-optimized the camera positions and the internal camera parameters to increase the accuracy of the model and computed additional matches between images to avoid bends or curves in the matched patches as recommended for projects including more than 500 images (Pix4Dmapper, 2022). In the second step, the 3D dense point cloud reconstruction was realized using the settings for medium quality and optimal point density. The densification was done using a matching 9×9 pixel window and an automatically limited camera depth in order to prevent the reconstruction of background objects. As a last step, we computed the photo orthomosaics and the DSMs based on the 3D dense point clouds. We used the built-in noise filtering and sharp surface smoothing algorithms of Pix4D. The DSMs were generated using the inverse distance weighting interpolation method.

3.2.2. DSM model error assessment

The error on the two DSMs was determined from the horizontal and vertical misfits between the two DSMs and the reference DSM, and based on the coordinates of the absolute, and relative GCPs. We calculated the average error, the standard deviation (SD) and the root mean square error (RMSE) in each x, y, z direction. The DSM was considered as calibrated when the average error (x, y and z) showed values below 0.1 m as suggested by Zhang et al. (2019) and Kalacska et al. (2020). Additionally, we compared the coordinates of checkpoints between the reference DSM and the resulting DSMs. We computed the average error, the SD and the RMSE to assess the errors of the models.

3.2.3. Comparison of co-registration and co-alignment techniques

For a subset of the images, we compared the performance of co-registration and co-alignment techniques for surface change detection. In contrast to the co-registration technique described above, the co-alignment methodology imports images from two different surveys into one single block (Cook and Dietze, 2019), and runs the first step of the SfM workflow, i.e., the image alignment, on the entire block without adding GCPs. Thereby, detected matching points are invariant and robust to distortions over time. After the image matching procedure, the co-alignment method separates the images of the different surveys but retains the position and camera calibration information. The remaining two steps of the SfM workflow, i.e., 3D point cloud and DSM computations, are completed on the images of each survey separately. We applied the co-alignment method to a subset of images covering a subset area of the gully in the alluvial fan in the southern part of the study area and obtained the DSM models for the three surveys and the DoDs. The uncertainty of the change detection was then compared with the outcome of the co-registration workflow that was described above.

3.3. Landscape change assessment

3.3.1. Spatially distributed uncertainty

The uncertainty of the elevation change assessment included the propagation of the identified errors into the DoD and the assessment of the significance of the DoD uncertainty. We used the probabilistic method described in Wheaton et al. (2010) and proposed earlier by Brasington et al. (2003) and Lane et al. (2003). The method estimates the critical threshold error, U_{crit}, (Eq. (1)), based on the standard deviation of the individual DSM model error (SDE) and a critical Student's t-value:

$$U_{crit} = t\left(\sqrt{SDE_1^2 + SDE_2^2}\right) \tag{1}$$

where SDE_1 and SDE_2 are the SDE for two different DSM models obtained at different moments.

Thus, we calculated the propagated error, and the probability of the predicted elevation change to occur, by relating the t-statistic to its cumulative distribution function at a selected confidence interval (more details in Wheaton et al., 2010). Based on that, the uncertainty can be spatially distributed over the area. We used the 95 % confidence interval as a threshold. Likewise, the DoD errors with probability values smaller than our threshold were discarded. Positive values corresponded to significant increases in elevation, while negative values represented significant surface lowering or erosion. The presented approach has been implemented in the Geomorphic Change Detection (GCD) add-in for ArcGIS (Bailey et al., 2020) and it was applied to our study using the high-resolution DSM models (~0.04 m pixel size).

3.3.2. Landscape change assessment

Elevational changes can be the result of land cover changes and geomorphic dynamics. In order to identify drivers of change, landscape units were classified in five main groups: infrastructure (paths, buildings, bridges and their embankments), vegetation (herbs, shrubs and trees, and riparian vegetation), cropland (fruit trees), bare or degraded land (bare land, river banks and floodplain) and water bodies (Cañete River). Using the high-resolution orthophotomosaics that were re-aligned after the co-registration step, we carried out object-based image classification which is recommended for high-resolution images. The software e-cognition, v. 9.01, (Trimble Geospatial) segments the orthophotomosaic in polygons, based on the shape, altitude and colour, to classify the different objects in the area. The performance of the object-based classification was assessed using a confusion matrix, based on 300 points randomly distributed over the study area. Likewise, we estimated the overall accuracy, user and producer accuracy, and kappa statistic of the classification.

We achieved a detailed analysis of the results, focusing on two areas with major landscape changes over the study period. Our analyses focussed on two major aspects of landscape change over the study period: (1) changes to infrastructure, vegetation and cropland associated with land cover changes, and (2) changes to bare and degraded land, and the Cañete River channel associated with geomorphic dynamics. We extracted the DoDs for each class (infrastructure, vegetation, cropland, bare and degraded land, and water body), and identified the magnitude and driver of landscape change.

4. Results

4.1. Consistency of image geotagging

The image coordinates and elevation were obtained in RTKLib by applying the PPK methodology. The analysis started with an elevation mask of 15° to include as much satellites as possible. The elevation mask value was then increased by small increments until the positions were fixed. Our results showed that 26 % of the coordinates were fixed with an elevation mask of 15° and 74 % with 20°. In parallel, we checked the accordance between fix-and-hold and continuous integer ambiguity resolution methods. For our study, 13 % of the positions were fixed by using the continuous method, and 87 % by fix-and-hold. The calculated image positions reflected the performance of the PPK methodology: the standard deviation (SD) of the coordinates and elevation presented millimetric values (Fig. 2). The average SD for the X axis and Y axis were 0.012 m and 0.008 m, respectively. For the Z axis, the SD reached a value of 0.019 m.

4.2. Surface DSM model errors

The DSM of the July 2019 survey showed the lowest misfit and highest consistency compared to the reconstructions for the February 2019 and March 2021 surveys and was therefore selected as the reference map (t_0). The GCPs and check points were positioned in the reference model (Fig. 1) and their coordinates extracted from the underlying photogrammetry. These coordinates were used for co-registration of the other point clouds. The resulting DSM models were renamed as t_{-5} for the February 2019 (−5 months) and t_{+20}, for March 2021 (+20 months) surveys (see Suppl. Materials S3).

The errors in the DSM models, relative to the reference model (t_0), were computed for all GCPs (light blue boxplots in Fig. 3a). The mean horizontal errors (X, Y) were smaller than 0.03 m for the t_{-5} model and around zero for the t_{+20} model. For the t_{-5} model, the mean elevation error (Z) was 0.031 m with a SD and a RMSE of 0.241 m; and for the t_{+20} model the mean elevation error was and 0.018 m with SD of 0.134 and a RMSE of 0.135 m. The external validation on the checkpoints (red boxplots) showed centimetric horizontal errors (X, Y) that are below 0.07 m for the t_{-5}, and below 0.05 m for the t_{+20} model; and mean elevation errors (Z) of 0.069 m for the t_{-5}, and 0.19 m for the t_{+20} model (Fig. 3).

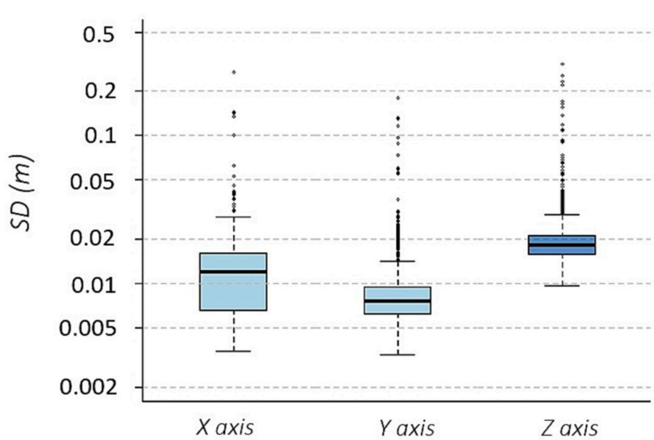

Fig. 2. Performance of the PPK image geotagging. The boxplots show the distribution of standard deviation (SD) in logarithmic scale of the calculated image coordinates (X and Y axis) and elevation (Z axis).

4.3. Comparison of co-registration and co-alignment methods

The results in the subset area of the ephemeral stream on the fan (Fig. 4a, b) revealed the performance quality of both co-registration by using relative GCPs, and co-alignment using information of multiple surveys (Fig. 4c to f). Using co-registration, 40 % of the pixels had a probability of change higher than |0.35| m (Fig. 4c and d). By applying co-alignment, 97 % of the subset area had a probability of change lower than |0.2| m (Fig. 4e), which is evident from the DoD map where topographic changes are hardly noticeable (Fig. 4f). We observed that 1.5 % of the subset area presented a probable change in elevation with co-registration, while only 0.06 % of the subset area was identified as probable of change with co-alignment. In the study area, the change detection based on co-registration outperformed that of the co-alignment technique.

4.4. Change detection: isolating geomorphic dynamics from land cover changes

By applying co-registration and by contrasting the raw and thresholded DoDs at 95 % confidence interval (Fig. 5a, b), our results showed that 32 % of the entire study area presented elevation changes between February 2019 and March 2021. The minimum elevation change observed was |0.56|m and the maximum |9.8| m. The object-based classification of the landscape units (Fig. 5c) presented a good performance of 88 % overall accuracy and a high kappa statistic of 87 % (see Suppl. Material S2). Overall, the 'cropland' and 'vegetation' classes are located in the alluvial valley while 'infrastructure' (such as roads and buildings) were located next to the river channel and the lower part of the alluvial fan. Bare and degraded land can be found on the alluvial fan surface and steep valley sides.

Drivers of elevation changes are twofold: (1) land cover changes related to human infrastructure, cropland activities and vegetation removal, and (2) geomorphic dynamics related to erosion and deposition on hillslopes, the alluvial fan, and ephemeral channels, and to valley scouring. Over the entire study area and over the 25-month period (2019–2021), 87 % of the pixels from the thresholded DOD (Fig. 5b) were related to land cover changes with an elevation change range of |1.6| m to |9.8| m and 13 % to geomorphic dynamics including an elevation change between |0.56| m and |3.2| m. The distal part of the alluvial fan and the lower valley floor were subject to land cover changes mostly related to rural infrastructure.

Regarding geomorphic dynamics, the most active feature was the ephemeral stream dissecting the alluvial fan (R1 in Fig. 5c; covering 5176 m^2). The intermittent stream is braided with low sinuosity, and widening of the channel was evidenced from erosion of its channel banks. Over the 25-month monitoring period, the channel widened as a result of channel migration. Undercutting and lateral bank erosion of ~0.75 to 3.2 m was the main mechanism of channel widening.

During the studied period about 83 m^3 of material was eroded, and efficiently transported downstream. There are no indications of net fluvial deposition in the ephemeral channel, but colluvial deposits were observed at the footslopes of the steep valley walls (Fig. 6a). These deposits with a volume of ~46 m^3 were the result of bank erosion and collapse of the valley wall (Fig. 6b–c). So, net sediment erosion was estimated at ~37 m^3 for the 5176 m^2 area, corresponding to 18.5 m^3 yr^{-1} or ~9500 t km^2 yr^{-1} (using a sediment density equal to 2.65 t m^{-3} for the unit conversion).

The Cañete River (R2 in Figs. 5c, 7) where the channel is constrained by the bridge (16 m width) is the second area of interest. Land cover changes resulting from vegetation dynamics were the main cause of the elevation changes (Fig. 7b) and they obscure the change related to geomorphic dynamics (Fig. 7a). The images illustrate the changes in the upper section of this area (northern area in Fig. 7b), where vegetation was removed for the construction of lateral embankments (made of boulders of ~1.2 m diameter). The (temporal) stability of the lower left

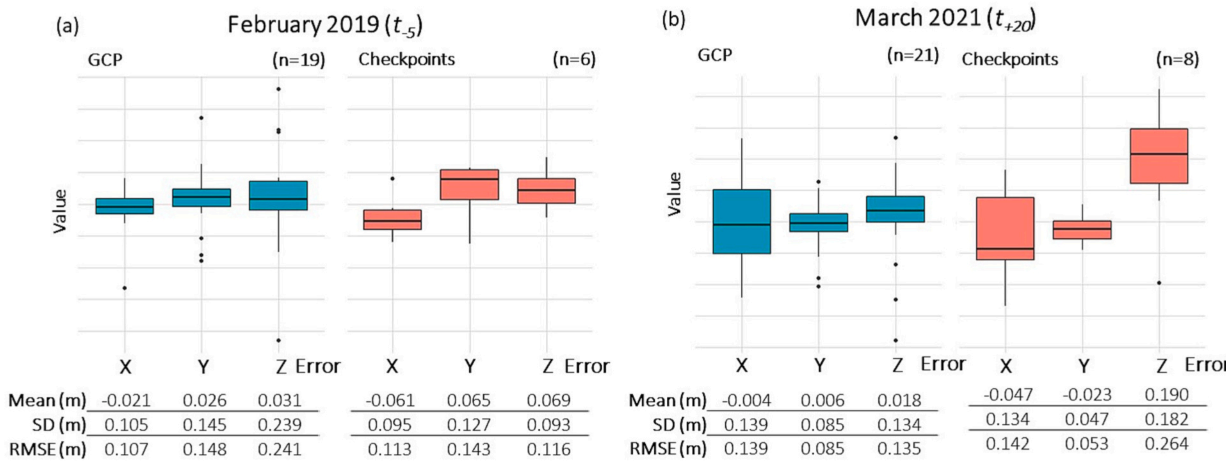

Fig. 3. Relative errors of the DSMs after co-registration: (a) February 2019, t_{-5}, and (b) March 2021, t_{+20}. The boxplots show the mean, SD and RMSE of planimetric (X, Y) and elevation (Z) errors of the GCPs and the check points. The n value represents the number of GCPs (blue) or checkpoints (red). (For interpretation of the references to colour in this figure legend, the reader is referred to the web version of this article.)

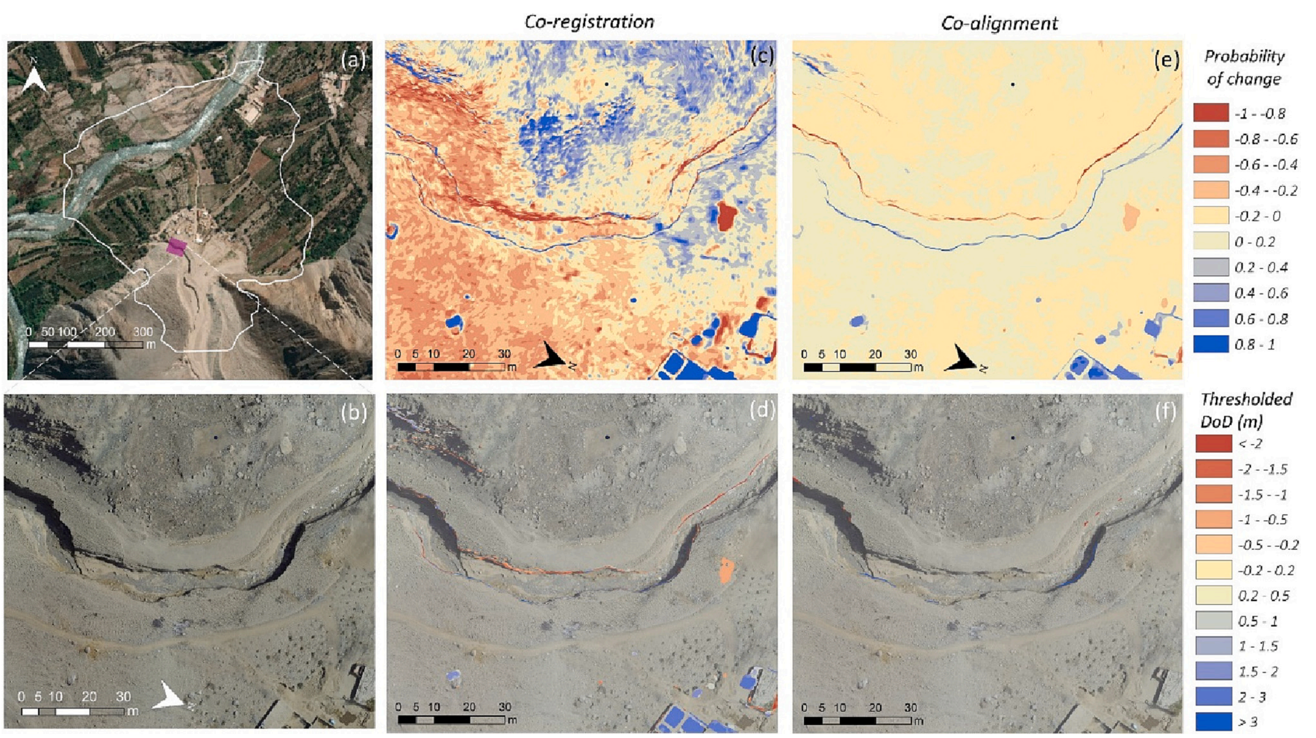

Fig. 4. Comparison between co-registration and co-alignment methods in the subset areas. (a) Location of the subset area (purple square) and (b) orthophotomosaic. (c, e) Spatial distribution of the probability of change in elevation. (d, f) Thresholded DoD. Negative and positive values denote probable surface lowering and rising. (For interpretation of the references to colour in this figure legend, the reader is referred to the web version of this article.)

bank was evidenced from vigorous plant growth (~+1.8 m) along the point bars (Fig. 7b). During the studied period, there was no evidence of bank erosion or channel migration, possibly due to natural and grey infrastructure that is preventing channel migration and bank erosion.

5. Discussion

5.1. Annual geomorphic change detection in (semi-)arid regions

This case study in the western Peruvian Andes shows that 4D models allow monitoring of geomorphic processes at dm-scale spatial resolution. Our original UAV-PPK-SfM dataset covered an area of ca. 0.3 km^2 and timespan of 2 years. The level of detection of surface deformations was adequate to detect changes that were larger than 0.56 m over the entire 25-month period. Even though our dataset did not allow an exhaustive assessment of sediment dynamics because of its limited size, we identified several hotspots of active erosion processes (Fig. 5b, c). The ephemeral channel is the most dynamic geomorphic feature in the area, and it is migrating rapidly. Our 4D analysis reveals that ephemeral streams can be very active geomorphic features, with channel widening and bank erosion rates of up to 1.6 m yr^{-1}, and 18.5 m^3 yr^{-1} or 9500 t km^{-2} yr^{-1} of eroded material (when using a sediment density equal to 2650 kg m^{-3} for the unit conversion), even in years with average precipitation rates of 15.1 mm yr^{-1} and absence of extreme weather events.

By providing quantitative data on surface elevation change in steep and mountainous areas located in the western Peruvian river basins, the

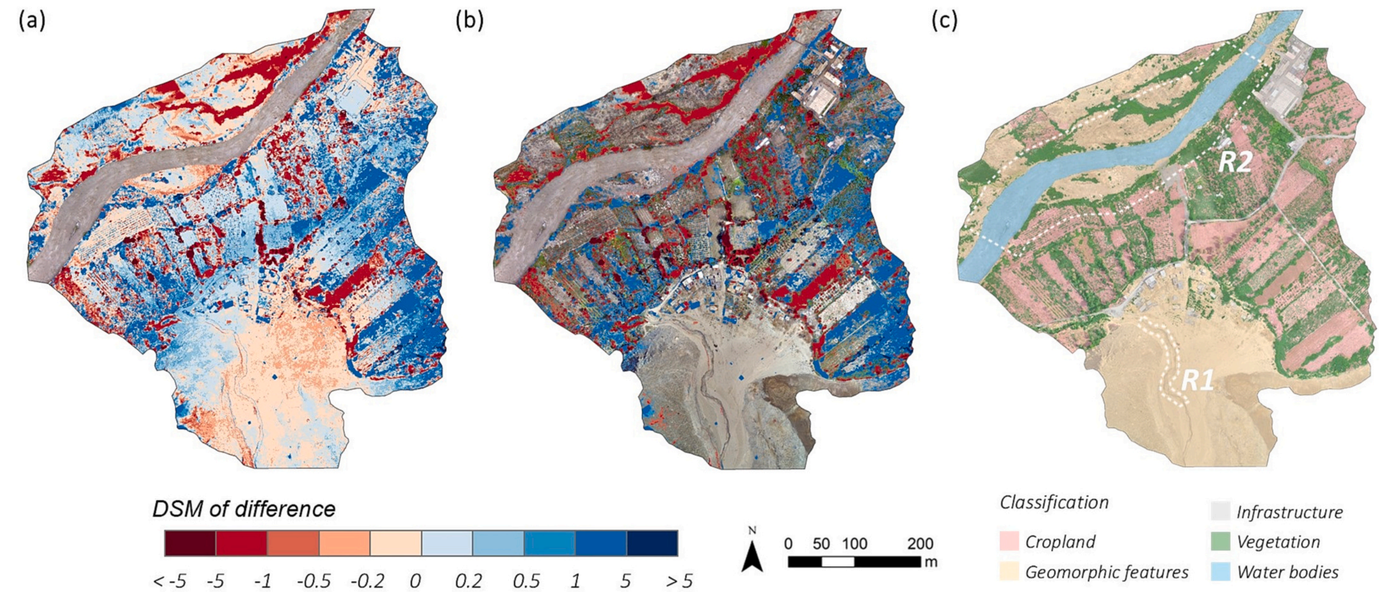

Fig. 5. DoDs between February 2019, t_{-5}, and March 2021, t_{+20}. (a) Visualization of raw DoD, and (b) thresholded DoD. (c) Object-based classification of landscape units with indication of the two selected regions (R1 and R2).

UAV-PPK-SfM approach contributed with new data on soil erosion rates and geomorphic change in river valleys, that is lacking for the western, arid Andes. Periods of intensive erosion and deposition are often uniquely linked to extreme climatic events such as ENSO-related extreme weather (Mettier et al., 2009; Tote et al., 2011; Morera et al., 2017). However, few quantitative data existed on geomorphic process rates at the event scale (INGEMMET, 2013). This case-study in the Cañete River valley exemplifies the magnitude of erosion events in ephemeral channels in the arid Andes. The calculated erosion rate of 9500 t km^{-2} yr^{-1} in the ephemeral channel greatly exceed the soil loss rates (2590 $\pm$ 295 t km^{-2} yr^{-1}) and specific sediment yields (up-to 2600 $\pm$ 570 t km^{-2} yr^{-1}) that were compiled for the Andes (Vanacker et al., 2022; Rosas et al., 2023).

Even though the applied methodology was not capable of assessing in more detail the anthropogenic drivers of geomorphic change in the area, the increased anthropogenic activity and land cover change in the region (Morris, 2017; Rosas et al., 2020) might further enhance or control geomorphic activity (Vanacker et al., 2022). The green and grey infrastructure along the river banks could reduce bank erosion and channel migration. On the other hand, the removal of natural vegetation to e.g., expand cultivated areas, can reduce soil protection and slope stability and potentially trigger soil erosion and sediment production by mass movements (Restrepo et al., 2015; Ochoa et al., 2016; Grima et al., 2020), and even reduce channel stability (Vanacker et al., 2005; Downs and Piégay, 2019). Given the rugged topography, eroded material may be effectively transported and potentially accumulated downstream as no net changes were observed in the elevation of the ephemeral channel bed.

The output is particularly relevant for the monitoring of concentrated geomorphic processes, such as lateral widening or migration of ephemeral channels and mass movements. These are hard to monitor with traditional surveying techniques because of the needed high resolution and the difficult access in steep mountainous terrain. The observed data can then be integrated with other soil erosion measurements, resulting from e.g. runoff/erosion plots (e.g., Inbar and Llerena, 2000; Molina et al., 2007; Ehrhardt et al., 2022), isotopic tracers (e.g., Fujiyoshi et al., 2009), gauging stations (e.g., Morera et al., 2017; Vanacker et al., 2020; Coviello et al., 2020) or sensors of mass movement detection (Simoni et al., 2020).

5.2. Performance of the co-registration approach: new perspectives

Recent advances in UAV-SfM techniques have made it possible to survey landscape morphology at m^2 to km^2-scale at a relatively low cost and with high time flexibility (Eltner et al., 2015). Previous 4D studies reported decimetric level of detection (LoD = 0.30 m) for mostly flat areas of around 0.1 km^2 (e.g., Clapuyt et al., 2017) and up to 0.01 m for small areas of 600 m^2 (e.g., Eltner et al., 2015). In mountainous environments, it is often not possible to distribute GCPs on very steep slopes or in unstable terrains, which is essential for model consistency (Clapuyt et al., 2016). Invariant features in the landscape (e.g. local infrastructure, big rocks) can then be used as an alternative, as relative GCPs. The geographic position of these features can be extracted from a reference surface to co-register digital surface models (Eltner et al., 2016). When using co-registration techniques, James and Varley (2012), Tuffen et al. (2013) and Piermattei et al. (2015) obtained decametric accuracies.

By implementing PPK in the UAV-PPK-SfM workflow, it is possible to reduce the uncertainty on the camera locations that are used for image geotagging, and reduce the RMSE on the DSM reconstructions (Tonkin and Midgley, 2016). Zhang et al. (2019) showed that it is possible to obtain a limit of difference of around 0.10 m even when no GCPs are used. However, this approach has mostly been applied to flat or undulating topography and for small spatial extents. Here, we added co-registration by relative GCPs to the UAV-PPK-SfM workflow to monitor a 0.3 km^2 study area, resulting in DSMs with a decimetric RMSE (~0.1 m and ~0.2 m) and a DoD with an average probability of 60 %. However, our minimum observable elevation change (0.56 m) was higher than earlier reported levels of detection. This could be due to the extensive study area (0.3 km^2), variable quality of individual surveys, or also the relatively low number of relative and absolute GCPs. In the case study, the number of invariant GCPs and checkpoints that could be detected in the area was limited to ~20 as a result of rapid anthropogenic change, vegetation growth, and accessibility. A higher density and better distribution of GCPs could further improve the quality of the change detection.

Recently, Cook and Dietze (2019) proposed co-alignment for 4D monitoring in rugged topography, and they reported planimetric and elevational errors of ~0.10 m. Similar results were obtained by de Haas et al. (2021) for the Illgraben torrent in the Swiss Alps. The co-alignment technique merges all images from all surveys and analyses them together. A key limitation hereby is that the number of matching

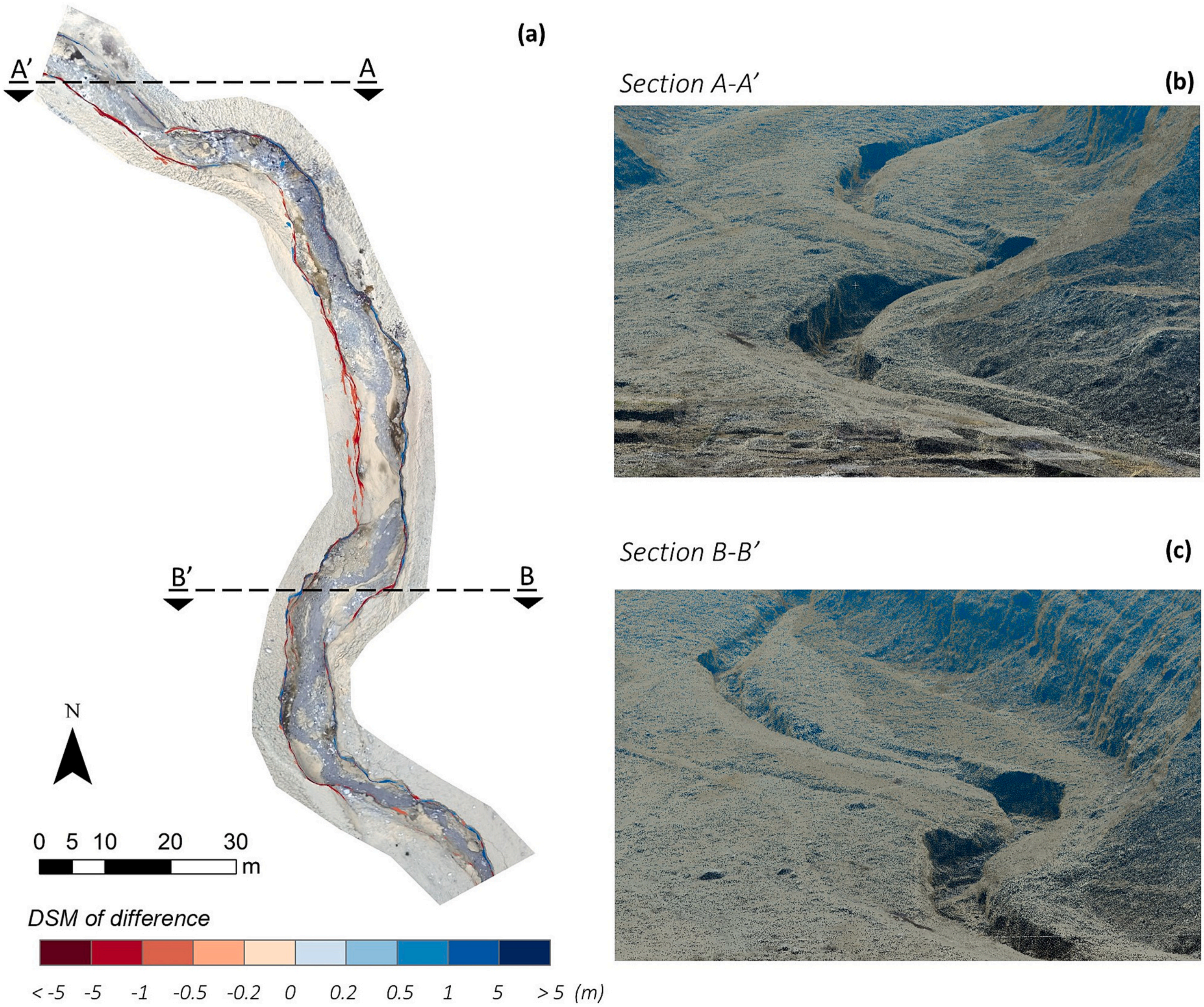

Fig. 6. Close-up view of the ephemeral stream (R1 in Fig. 5). (a) Thresholded DoD with 95 % confidence interval. The colour bar shows the vertical changes in meters. The images on the right show a 3D impression of (b) A-A′ and (c) B-B′ cross sections.

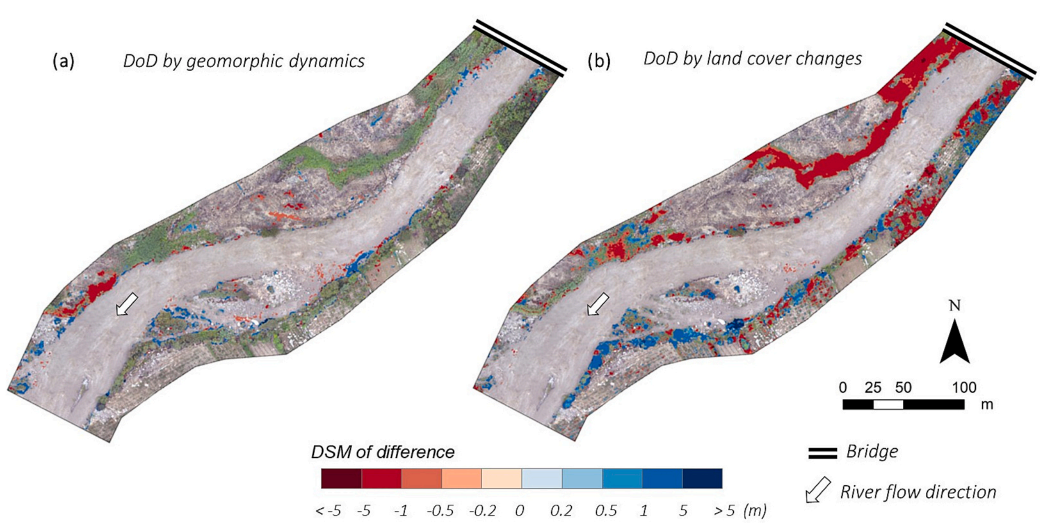

Fig. 7. Close-up of the Cañete River channel (R2 in Fig. 5). Thresholded DoD with 95 % confidence interval. (a) Geomorphic dynamics and (b) land cover changes. The colour bar shows the vertical changes in surface elevation (in meters).

tiepoints may not be sufficient when important landscape changes occur between surveys, for example as the result of geomorphic events such as mass movements or floods. In such situations, additional GCPs are needed (Cook and Dietze, 2019; Hendrickx et al., 2020). We compared the outcomes of co-registration and co-alignment for a subset area (Fig. 4) that was characterised by rapid landscape change. Besides the fact that the photogrammetric processing time is significantly longer for co-alignment because of the large quantity of images that need to be processed together when merging surveys, the change detection based on co-registration outperformed the results of the co-alignment technique.

6. Conclusions

Given the dynamic geomorphology of the western Peruvian Andes and its exposure to accelerated environmental change, there is an urgent need to identify hotspots of geomorphic change and quantify erosion, sediment production, and delivery to the channel network. This case study demonstrated the potential of uncrewed aerial vehicles to monitor 4D landscape changes and to quantify geomorphic process rates in river valleys. By including co-registration of point clouds by means of relative GCPs in the image processing workflow, we were able to pinpoint hotspots of geomorphic change undergoing probable elevation changes above 0.56 m (95 % confidence interval). An object-based land cover classification allowed us to separate geomorphic dynamics from land cover changes. Ephemeral streams were identified as the hotspots of geomorphic activity: the widening of the valley floor took place at rates of 0.3 to 1.6 m yr^{-1} as a result of river undercutting and bank erosion, and 18 m^3 yr^{-1} of material has been exported downstream corresponding to a specific sediment yield of about 9500 t km^{-2} yr^{-1}. The monitoring period covered only average, interannual weather events, and it illustrated that erosion rates may be underestimated in ungauged river basins along the western Peruvian Andes.

CRediT authorship contribution statement

The project was designed by VV and MR. The UAV flights were done by MR, and WV contributed with georeferencing GCPs and field trip logistics. The UAV-PPK-SfM workflow with co-registration was developed by VV, MR and FC. Funding acquisition was done by MR, WV and VV. The paper was written by MR, VV, FC and WV. All authors reviewed and approved the paper.

Declaration of competing interest

The authors declare that they have no known competing financial interests or personal relationships that could have appeared to influence the work reported in this paper.

Data availability

Data will be made available on request.

Acknowledgements

The research was supported by the Belgian Académie de recherche et d'enseignement supérieur (ARES) as part of the POP project “Erosion and sediment yield in response to climate change and variability in Andean watersheds” awarded to VV and WV. MR was awarded the “Fondos no concursables de apoyo a la investigacion 2019 (FONCAI-0012-2019)” from the Pontificia Universidad Católica del Perú. MR received a PhD Scholarship from the Conseil de l'Action Internationale from UCLouvain (Grant No. ADRI/CD/CA/2016-NR 51) and the ARES-CCD in 2021. FC acknowledges funding from the Fonds de la Recherche Scientique (FRS-FNRS). The authors thank Carlos Yaya for his collaboration in the field campaigns. The insightful and constructive reviews by Mike James, Christopher Neil Gibbins, an anonymous reviewer and editor Yuichi S. Hayakawa were very helpful in improving the quality of this manuscript.

Appendix A. Supplementary data

Supplementary data to this article can be found online at https://doi.org/10.1016/j.geomorph.2023.108766.

References

Aber, J.S., Marzolff, I., Ries, J.B., Aber, S., 2019. Chapter 16 - vegetation, soil, and soil erosion. In: Thomson, E. (Ed.), Small-Format Aerial Photography and UAS Imagery Principles, Techniques, and Geoscience Applications, 2nd edition, pp. 291–305. https://doi.org/10.1016/B978-0-12-812942-5.00016-1.

Aybar, C., Fernandez, C., Huerta, A., Lavado, W., Vega, F., Felipe-Obando, O., 2020. Construction of a high-resolution gridded rainfall dataset for Peru from 1981 to the present day. Hydrol. Sci. J. 65 (5), 770–785. https://doi.org/10.1080/02626667.2019.1649411.

Bailey, P., Wheaton, J., Reimer, M., Brasington, J., 2020. Geomorphic Change Detection Software (7.5.0). Zenodo. https://doi.org/10.5281/zenodo.7248344.

Barrowclough, M., Stehouwer, R., Alwang, J., Gallagher, R., Barrera Mosquera, V.H., Domínguez, J.M., 2016. Conservation agriculture on steep slopes in the Andes: promise and obstacles. J. Soil Water Conserv. 71 (2), 91–102. https://doi.org/10.2489/jswc.71.2.91.

Brasington, J., Langham, J., Rumsby, B., 2003. Methodological sensitivity of morphometric estimates of coarse fluvial sediment transport. Geomorphology 53 (3–4), 299–316. https://doi.org/10.1016/S0169-555X(02)00320-3.

Cândido, B.M., Quinton, J.N., James, M.R., Silva, M.L.N., de Carvalho, T., de Lima, W., Beniaich, A., Eltner, A., 2020. High-resolution monitoring of diffuse (sheet or interrill) erosion using structure-from-motion. Geoderma 375, 114477. https://doi.org/10.1016/j.geoderma.2020.114477.

Clapuyt, F., Vanacker, V., Van Oost, K., 2016. Reproducibility of UAV-based earth topography reconstructions based on Structure-from-Motion algorithms. Geomorphology 260, 4–15. https://doi.org/10.1016/j.geomorph.2015.05.011.

Clapuyt, F., Vanacker, V., Schlunegger, F., Van Oost, K., 2017. Unravelling earth flow dynamics with 3-D time series derived from UAV-SfM models. Earth Surf. Dynam. 5, 791–806. https://doi.org/10.5194/esurf-5-791-2017.

Clark, K.E., West, A.J., Hilton, R.G., Asner, G.P., Quesada, C.A., Silman, M.R., Saatchi, S. S., Farfan-Rios, W., Martin, R.E., Horwath, A.B., Halladay, K., New, M., Malhi, Y., 2016. Storm-triggered landslides in the Peruvian Andes and implications for topography, carbon cycles, and biodiversity, Earth Surf. Dynam. 4, 47–70. https://doi.org/10.5194/esurf-4-47-2016.

Cook, K.L., Dietze, M., 2019. Short Communication: a simple workflow for robust low-cost UAV-derived change detection without ground control points. Earth Surf. Dynam. 7, 1009–1017. https://doi.org/10.5194/esurf-7-1009-2019.

Coviello, V., Theule, J.I., Crema, S., Arattano, M., Comiti, F., Cavalli, M., Lucía, A., Macconi, P., Marchi, L., 2020. Combining Instrumental monitoring and high-resolution topography for estimating sediment yield in a debris-flow catchment. Environ. Eng. Geosci. 27 (1), 95–111. https://doi.org/10.2113/EEG-D-20-00025.

Cucchiaro, S., Fallu, D.J., Zhang, H., Walsh, K., Van Oost, K., Brown, A.G., Tarolli, P., 2020. Multiplatform-SfM and TLS data fusion for monitoring agricultural terraces in complex topographic and landcover conditions. Remote Sens. 12, 1946. https://doi.org/10.3390/rs12121946.

de Haas, T., Nijland, W., McArdell, B.W., Kalthof, M.W.M.L., 2021. Case report: optimization of topographic change detection with UAV structure-from-motion photogrammetry through survey co-alignment. Front. Remote Sens. 2, 626810 https://doi.org/10.3389/frsen.2021.626810.

Downs, P.W., Piégay, H., 2019. Catchment-scale cumulative impact of human activities on river channels in the late Anthropocene: implications, limitations, prospect. Geomorphology 338, 88–104. https://doi.org/10.1016/j.geomorph.2019.03.021.

Ehrhardt, A., Deumlich, D., Gerke, H.H., 2022. Soil surface micro-topography by structure-from-motion photogrammetry for monitoring density and erosion dynamics. Front. Environ. Sci. 9, 737702 https://doi.org/10.3389/fenvs.2021.737702.

Eker, R., Aydın, A., Hübl, J., 2018. Unmanned aerial vehicle (UAV)-based monitoring of a landslide: Gallenzerkogel landslide (Ybbs-Lower Austria) case study. Environ. Monit. Assess. 190, 28. https://doi.org/10.1007/s10661-017-6402-8.

Eltner, A., Baumgart, P., Maas, H., Faust, D., 2015. Multi-temporal UAV data for automatic measurement of rill and interrill erosion on loess soil. Earth Surf. Process. Landforms 40, 741–755. https://doi.org/10.1002/esp.3673.

Eltner, A., Kaiser, A., Castillo, C., Rock, G., Neugirg, F., Abellán, A., 2016. Image-based surface reconstruction in geomorphometry – merits, limits and developments. Earth Surf. Dynam. 4, 359–389. https://doi.org/10.5194/esurf-4-359-2016.

FAO, Food and Agriculture Organization of the United Nations, CAF, Corporación Andina de Fomento, 2016. Peru, Nota de Análisis Sectorial Agricultura y Desarrollo Rural.

Forlani, G., Dall'Asta, E., Diotri, F., Cella, U.M.D., Roncella, R., Santise, M., 2018. Quality assessment of DSMs produced from UAV flights georeferenced with on-board RTK positioning. Remote Sens. 2018 (10), 311. https://doi.org/10.3390/rs10020311.

Fujiyoshi, R., Satake, Y., Sato, T., Sumiyoshi, T., Dietz, J., Zimmermann, R., 2009. Natural and anthropogenic consequences of tropical forest soils in Northern Peru using environmental radionuclides as radiotracers. J. Radioanal. Nucl. Chem. 279, 509–518. https://doi.org/10.1007/s10967-007-7308-2.

Gonzáles-Moradas, M.D.R., Viveen, W., 2020. Evaluation of ASTER GDEM2, SRTMv3.0, ALOS AW3D30 and TanDEM-X DEMs for the Peruvian Andes against highly accurate GNSS ground control points and geomorphological-hydrological metrics. Rem. Sens. Environ. 237, 111509 https://doi.org/10.1016/j.rse.2019.111509.

Grima, N., Edwards, N., Edwards, F., Petley, D., Fisher, B., 2020. Landslides in the Andes: Forests can provide cost-effective landslide regulation services. Sci. Total Environ. 745, 141128 https://doi.org/10.1016/j.scitotenv.2020.141128.

Hendrickx, H., De Sloover, L., Stal, C., Delaloye, R., Nyssen, J., Frankl, A., 2020. Talus slope geomorphology investigated at multiple time scales from high-resolution topographic surveys and historical aerial photographs (Sanetsch Pass, Switzerland). Earth Surf. Process. Landforms 45, 3653–3669. https://doi.org/10.1002/esp.4989.

Höfle, B., Griesbaum, L., Forbriger, M., 2013. GIS-based detection of gullies in terrestrial LiDAR data of the Cerro Llamoca Peatland (Peru). Remote Sens. 5 (11), 5851–5870. https://doi.org/10.3390/rs5115851.

Huang, H., Long, J., Lin, H., Zhang, L., Yi, W., Lei, B., 2017. Unmanned aerial vehicle based remote sensing method for monitoring a steep mountainous slope in the Three Gorges Reservoir, China. Earth. Sci. Inform. 10, 287–301. https://doi.org/10.1007/s12145-017-0291-9.

Inbar, M., Llerena, C.A., 2000. Erosion processes in high mountain agricultural terraces in Peru. Mt. Res. Dev. 20, 72–79. https://doi.org/10.1659/0276-4741(2000)020[0072:EPIHMA]2.0.CO;2.

INGEMMET, 2013. GEOCATMIN: Peligros Geológicos del Peru. http://metadatos.ingemmet.gob.pe:8080/geonetwork/srv/spa/catalog.search#/metadata/c5580ab5-7277-4858-8d16-a982bd2cc23b. (Accessed May 2022).

INGEMMET, 2022. Boletín Ingemmet. Serie C: Geodinámica e Ingeniería Geológica. https://repositorio.ingemmet.gob.pe/handle/20.500.12544/8/?locale=en. (Accessed May 2022).

James, M.R., Robson, S., 2014. Mitigating systematic error in topographic models derived from UAV and ground-based image networks. Earth Surf. Process. Landforms 39, 1413–1420. https://doi.org/10.1002/esp.3609.

James, M.R., Varley, N., 2012. Identification of structural controls in an active lava dome with high resolution DEMs: Volcán de Colima, Mexico. Geophys. Res. Lett. 39, L22303. https://doi.org/10.1029/2012GL054245.

James, M.R., Chandler, J.H., Eltner, A., Fraser, C., Miller, P.E., Mills, J.P., Noble, T., Robson, S., Lane, S.N., 2019. Guidelines on the use of structure-from-motion photogrammetry in geomorphic research. Earth Surf. Process. Landforms 44, 2081–2084. https://doi.org/10.1002/esp.4637.

Kalacska, M., Lucanus, O., Arroyo-Mora, J.P., Laliberté, É., Elmer, K., Leblanc, G., Groves, A., 2020. Accuracy of 3D landscape reconstruction without ground control points using different UAS platforms. Drones 4 (2), 13. https://doi.org/10.3390/drones4020013.

Lacroix, P., Dehecq, A., Taipe, E., 2020. Irrigation-triggered landslides in a Peruvian desert caused by modern intensive farming. Nat. Geosci. 13, 56–60. https://doi.org/10.1038/s41561-019-0500-x.

Lane, S.N., Westaway, R.M., Hicks, D.M., 2003. Estimation of erosion and deposition volumes in a large, gravel-bed, braided river using synoptic remote sensing. Earth Surf. Process. Landf. 28 (3), 249–271. https://doi.org/10.1002/esp.483.

Latrubesse, E.M., Restrepo, J.D., 2014. Sediment yield along the Andes: Continental budget, regional variations, and comparisons with other basins from orogenic mountain belts. Geomorphology 216, 225–233. https://doi.org/10.1016/j.geomorph.2014.04.007.

Luque, G., Rosado, M., Pari, W., Peña, F., Huamán, M., 2020. Peligro geológico en la región Lima. INGEMMET Bol. Ser. C Geodinámica 76, 298 p., 9 mapas. https://hdl.handle.net/20.500.12544/2571.

Mettier, R., Schlunegger, F., Schneider, H., Rieke-Zapp, D., Schwab, M., 2009. Relationships between landscape morphology, climate and surface erosion in northern Peru at 5°S latitude. Int. J. Earth Sci. (Geol. Rundsch.) 98, 2009. https://doi.org/10.1007/s00531-008-0355-7.

Molina, A., Govers, G., Vanacker, V., Poesen, J., Zeelmaekers, E., Cisneros, F., 2007. Runoff generation in a degraded Andean ecosystem: interaction of vegetation cover and land use. Catena 71, 357–370. https://doi.org/10.1016/j.catena.2007.04.002.

Molina, A., Govers, G., Poesen, J., Van Hemelryck, H., De Bièvre, B., Vanacker, V., 2008. Environmental factors controlling spatial variation in sediment yield in a central Andean Mountain area. Geomorphology 98 (3–4), 176–186. https://doi.org/10.1016/j.geomorph.2006.12.025.

Morera, S.B., Condom, T., Crave, A., Steer, P., Guyot, J.L., 2017. The impact of extreme El Niño events on modern sediment transport along the western Peruvian Andes (1968–2012). Sci. Rep. 7, 11947. https://doi.org/10.1038/s41598-017-12220-x.

Morris, M., 2017. Gaining Momentum in Peruvian Agriculture: Opportunities to Increase Productivity and Enhance Competitiveness (English). World Bank Group, Washington, D.C.. http://documents.worldbank.org/curated/en/107451498513689693/Gaining-momentum-in-Peruvian-agriculture-opportunities-to-increase-productivity-and-enhance-competitiveness. (Accessed May 2022)

Nesbit, P.R., Hugenholtz, C.H., 2019. Enhancing UAV–SfM 3D model accuracy in high-relief landscapes by incorporating oblique images. Remote Sens. 11, 239. https://doi.org/10.3390/rs11030239.

Notti, D., Giordan, D., Cina, A., Manzino, A., Maschio, P., Bendea, I.H., 2021. Debris flow and rockslide analysis with advanced photogrammetry techniques based on high-resolution RPAS data. Ponte Formazza Case Study (NW Alps). Remote Sensing 13 (9), 1797. https://doi.org/10.3390/rs13091797.

Ochoa, P.A., Fries, A., Mejía, D., Burneo, J.I., Ruíz-Sinoga, J.D., Cerdà, A., 2016. Effects of climate, land cover and topography on soil erosion risk in a semiarid basin of the Andes. CATENA 140, 31–42. https://doi.org/10.1016/j.catena.2016.01.011.

Passalacqua, P., Belmont, P., Staley, D.M., et al., 2015. Analyzing high resolution topography for advancing the understanding of mass and energy transfer through landscapes: a review. Earth Sci. Rev. 148, 174–193. https://doi.org/10.1016/j.earscirev.2015.05.012.

Piermattei, L., Carturan, L., Guarnieri, A., 2015. Use of terrestrial photogrammetry based on structure-from-motion for mass balance estimation of a small glacier in the Italian alps. Earth Surf. Process. Landforms 40, 1791–1802. https://doi.org/10.1002/esp.3756.

Pingel, T.J., Saavedra, A., Cobo, L., 2021. Deriving land and water surface elevations in the Northeastern Yucatán Peninsula using PPK GPS and UAV-based structure from motion. Papers Appl. Geogr. 7 (3), 294–315. https://doi.org/10.1080/23754931.2021.1871937.

Pix4Dmapper, 2021. Professional photogrammetry and drone mapping software. Version 4.7. https://www.pix4d.com. (Accessed 12 November 2021).

Pix4Dmapper, 2022. Pix4D mapper documentation. https://support.pix4d.com/hc/en-us/articles/202559359-Difference-between-%22Reoptimize%22-and-%22Rematch-and-Optimize%22 (last accessed 13 June 2022).

Rau, P., Bourrel, L., Labat, D., Melo, P., Dewitte, B., Frappart, F., Lavado, W., Felipe, O., 2017. Regionalization of rainfall over the Peruvian Pacific slope and coast. Int. J. Climatol. 37, 143–158. https://doi.org/10.1002/joc.4693.

Rau, P., Bourrel, L., Labat, D., Frappart, F., Reulland, D., Lavado, W., Dewitte, B., Felipe, O., 2018. Hydroclimatic change disparity of Peruvian Pacific drainage catchments. Theor. Appl. Climatol. 134, 139–153. https://doi.org/10.1007/s00704-017-2263-x.

Restrepo, J.D., Lopez, S.A., Restrepo, J.C., 2009. The effects of geomorphic controls on sediment yield in the Andean rivers of Colombia. Latin Am. J. Sedimentol. Basin Anal. 16 (2), 79–92. https://lajsba.sedimentologia.org.ar/index.php/lajsba/article/view/107.

Restrepo, J.D., Kettner, A.J., Syvitski, J.P.M., 2015. Recent deforestation causes rapid increase in river sediment load in the Colombian Andes. Anthropocene 10, 13–28. https://doi.org/10.1016/j.ancene.2015.09.001.

Restrepo, J.D., Kettner, A.J., Brakenridge, G.R., 2020. Monitoring water discharge and floodplain connectivity for the Northern Andes utilizing satellite data: a tool for river planning and science-based decision-making. J. Hydrol. 590, 125123 https://doi.org/10.1016/j.jhydrol.2020.125123.

Rosas, M.A., Vanacker, V., Viveen, W., Gutierrez, R.R., Huggel, C., 2020. The potential impact of climate variability on siltation of Andean reservoirs. J. Hydrol. 581, 124396 https://doi.org/10.1016/j.jhydrol.2019.124396.

Rosas, M.A., Viveen, W., Vanacker, V., 2023. Spatial variation in specific sediment yield along the Peruvian western Andes. Catena 220, 106699. https://doi.org/10.1016/j.catena.2022.106699.

Schildgen, T.F., Hodges, K.V., Whipple, K.X., Reiners, P.W., Pringle, M.S., 2007. Uplift of the western margin of the Andean plateau revealed from canyon incision history, southern Peru. Geology 35 (6), 523–526. https://doi.org/10.1130/G23532A.1.

Simoni, A., Bernard, M., Berti, M., Boreggio, M., Lanzoni, S., Stancanelli, L.M., Gregoretti, C., 2020. Runoff-generated debris flows: Observation of initiation conditions and erosion–deposition dynamics along the channel at Cancia (eastern Italian Alps). Earth Surf. Process. Landforms 45, 3556–3571. https://doi.org/10.1002/esp.4981.

Takasu, T., Yasuda, A., 2009. Development of the low-cost RTKGPS receiver with an open source program package RTKLIB. In: International Symposium on GPS/GNSS, 4–6 November 2009, Jeju, Korea.

Tarolli, P., 2014. High-resolution topography for understanding Earth surface processes: opportunities and challenges. Geomorphology 216, 295–312. https://doi.org/10.1016/j.geomorph.2014.03.008.

Tonkin, T.N., Midgley, N.G., 2016. Ground-control networks for image based surface reconstruction: an Investigation of optimum survey designs using UAV derived imagery and structure-from-motion photogrammetry. Remote Sens. 8, 786. https://doi.org/10.3390/rs8090786.

Tote, C., Govers, G., Van Kerckhoven, S., Filiberto, I., Verstraeten, G., Eerens, H., 2011. Effect of ENSO events on sediment production in a large coastal basin in northern Peru. Earth Surf. Process. Landforms 36, 1776–1788. https://doi.org/10.1002/esp.2200.

Trimble Geospatial. Trimble eCognition, version 9.0.1. https://geospatial.trimble.com/products-and-solutions/ecognition (accessed 12 November 2021).

Tuffen, H., James, M.R., Castro, J.M., Schipper, C.I., 2013. Exceptional mobility of a rhyolitic obsidian flow: observations from Cordón Caulle, Chile, 2011–2013. Nat. Comms. 4, 2709. https://doi.org/10.1038/ncomms3709.

Vanacker, V., Govers, G., Poesen, J., Deckers, J., Dercon, G., Loaiza, G., 2003. The impact of environmental change on the intensity and spatial pattern of water erosion in a semi-arid mountainous Andean environment. CATENA 51 (3–4), 329–347. https://doi.org/10.1016/S0341-8162(02)00172-8.

Vanacker, V., Molina, A., Govers, G., Poesen, J., Dercon, G., Deckers, S., 2005. River channel response to short-term human-induced change in landscape connectivity in Andean ecosystems. Geomorphology 72 (1–4), 340–353. https://doi.org/10.1016/j.geomorph.2005.05.013.

Vanacker, V., Guns, M., Clapuyt, F., Balthazar, V., Tenorio, G., Molina, A., 2020. Distribución espacio-temporal de los deslizamientos y erosión hídrica en una cuenca Andina tropical. Pirineos 175, e051. https://doi.org/10.3989/pirineos.2020.175001.

Vanacker, V., Molina, A., Rosas-Barturen, M., Bonnesoeur, V., Román-Dañobeytia, F., Ochoa-Tocachi, B.F., Buytaert, W., 2022. The effect of natural infrastructure on water erosion mitigation in the Andes. SOIL 8, 133–147. https://doi.org/10.5194/soil-8-133-2022.

Viveen, W., Sanjurjo-Sanchez, J., Rosas, M.A., Vanacker, V., Villegas-Lanza, J.C., 2022. Heinrich events and tectonic uplift as possible drivers for late Quaternary fluvial dynamics in the western Peruvian Andes. Glob. Planet. Chang. 218, 103972.

Wackrow, R., Chandler, J.H., 2008. A convergent image configuration for DEM extraction that minimises the systematic effects caused by an inaccurate lens model. Photogrammetric Record 23, 6–18. https://doi.org/10.1111/j.1477-9730.2008.00467.x.

Wheaton, J.M., Brasington, J., Darby, S.E., Sear, D.A., 2010. Accounting for uncertainty in DEMs from repeat topographic surveys: improved sediment budgets. Earth Surf. Process. Landforms 35, 136–156. https://doi.org/10.1002/esp.1886.

Žabota, B., Kobal, M., 2021. Accuracy assessment of UAV-photogrammetric-derived products using PPK and GCPs in challenging terrains: in search of optimized rockfall mapping. Remote Sens. 13 (19), 3812. https://doi.org/10.3390/rs13193812.

Zerathe, S., Lacroix, P., Jongmans, D., Marino, J., Taipe, E., Wathelet, M., Pari, W., Smoll, L.F., Norabuena, E., Guillier, B., Tatard, L., 2016. Morphology, structure, and kinematics of a rainfall controlled slow-moving Andean landslide, Peru. Earth Surf. Process. Landforms 41, 1477–1493. https://doi.org/10.1002/esp.3913.

Zhang, H., Aldana-Jague, E., Clapuyt, F., Wilken, F., Vanacker, V., Van Oost, K., 2019. Evaluating the potential of post-processing kinematic (PPK) georeferencing for UAV-based structure-from-motion (SfM) photogrammetry and surface change detection. Earth Surf. Dynam. 7, 807–827. https://doi.org/10.5194/esurf-7-807-2019.